Electronic coherences steer the strong isotope effect in the ultrafast Jahn-Teller structural rearrangement of methane cation upon tunnel ionization

Martin Blavier,[1] Ksenia Komarova,[2] Cayo E. M. Gonçalves,[1] R. D. Levine,[2,3] F. Remacle[1,2]

[1]Theoretical Physical Chemistry, University of Liège, 4000 Liège, Belgium
[2]The Fritz Haber Research Center for Molecular Dynamics, The Hebrew University of Jerusalem, 91904 Jerusalem, Israel
[3] Department of Chemistry and Biochemistry and Department of Molecular and Medical Pharmacology, David Geffen School of Medicine, University of California, Los Angeles, CA 90095, USA

Abstract

We report on fully quantum electronic-nuclear dynamics following sudden ionization from the neutral in the three lowest electronic states of the CH_4^+ and CD_4^+ cations. There is a strong Jahn-Teller effect in the Franck-Condon region and we employ two nuclear degrees of freedom that span the internal coordinates involved in the Jahn-Teller coupling. The initial state results from tunneling ionization by a strong IR field which coherently pumps the three lowest states of the cation, D_0, D_1 and D_2. The quantum dynamical simulations show that a strong isotope effect occurs when the ionization accesses significantly the D_2 state of the cation in the Franck-Condon region. The computed isotope effect is larger than expected on the basis of the effective mass ratio. The strong effect is due to fast oscillations of the electronic coherences between the D_2 and the D_1 and D_0 electronic states and their modulation by the non adiabatic couplings before a significant onset of nuclear motion. The magnitude of the effect is similar to the one that we previously reported for a sudden photoionization process. A strong isotope effect has been observed in high harmonic spectroscopy studies of the very short time dynamics Jahn-Teller structural rearrangement of the methane cation upon sudden ionization.

CH_4^+/CD_4^+
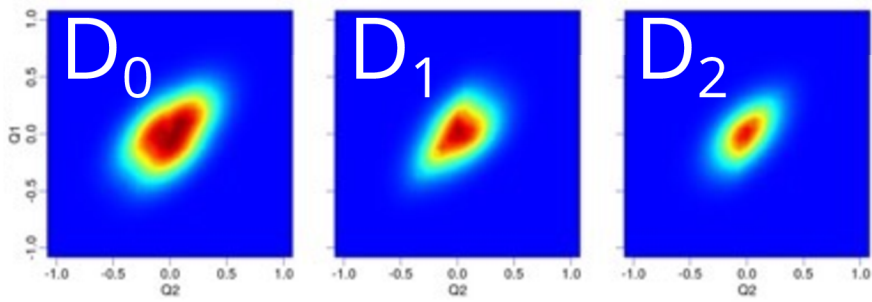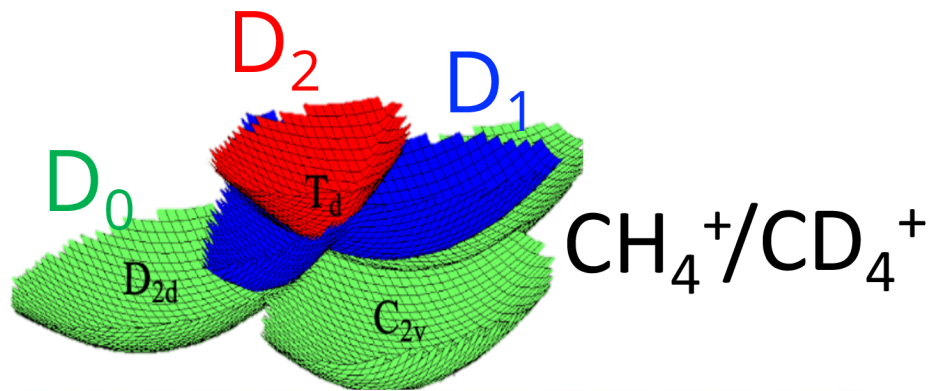
Introduction

The progress in the engineering of atto and few femtosecond optical pulses[1-6] provides access to initiating, controlling and probing electronic coherences in molecular systems.[7-10] Electronic coherences are built upon photoexcitation or photo or tunneling ionization when several electronic states are simultaneously and coherently accessed. This is made possible by the broad energy band width of short sub fs or atto pulses. The non stationary superposition of electronic and vibrational states built by the excitation process then evolves coherently on the potentials of the different electronic states where it encounters regions of non adiabatic couplings between electronic states that is driven by the nuclear motion. In this new intrinsically post Born and Oppenheimer regime, not only nuclei but also electrons are out of equilibrium in the initially pumped state.[10-11] The new aspect brought by the post Born-Oppenheimer regime is the formation of electronic coherences at the excitation step which modulate the temporal and spatial localization of the electronic density in the molecule. As the dynamics unfold, new electronic states and new nuclear modes are brought in by the non adiabatic and anharmonic couplings. One of the challenges of attochemistry is to devise control schemes that exploit the electronic coherences built at the excitation step to steer the nuclei towards specific products.

A particularly interesting case for studying the role of electronic coherences built at the excitation step is when the regions of non adiabatic coupling are localized in the Franck-Condon region or in its close vicinity. A text book example of such a situation is the Jahn-Teller rearrangement that occurs in the methane cation upon sudden ionization of the neutral. The sudden ionization creates a superposition of those three electronic states of the cation that are degenerate at the equilibrium T_d geometry of the neutral molecule. In the cation, the T_d geometry is unstable because of the Jahn-Teller (JT) effect which induces a structural rearrangement to a geometry of a lower symmetry. The rearrangement is ultrafast. It occurs in a very few fs's through strong non adiabatic couplings between the three electronic states in the Franck-Condon region where the electronic and nuclear motions are strongly correlated. The JT rearrangement is therefore significantly affected by isotopic substitution. A pioneering study by High Harmonic Spectroscopy indeed reports a strong isotope effect, larger than expected on the basis of the effective mass ratio, in the first ≈ 1.6 fs of the dynamics.[12-13] This experimental result stimulated several theoretical studies[14-18] The yield in high harmonics has been shown to be proportional to the autocorrelation function, $\left|C(t)\right|^2$, of the initial state of the

cation.[19] The reason for the isotope effect is attributed to the slower motion out of the Franck-Condon region of CD_4^+ with respect to CH_4^+ which leads to a higher yield in harmonics when the electron recombines with the cation. Theoretical studies therefore compare the ratio of the autocorrelation of the initial state of the two isotopomers to the ratio of the yields in harmonics. Mondal and Varandas reported MCTDH computations for a quasi vibronic coupling model in the three lowest states of the methane cation with increasing nuclear dimensionality up to the full 9 dimensionality.[16-18] Their computations show that 5 nuclear degrees of freedom, the t_2 mode and the e mode of the T_d geometry that are strongly involved in the Jahn-Teller effect are necessary to account for the large experimental isotope effect.[18] In these computations, the ionization process is not described in details and the three electronic states are populated uniformly in the geometries of the Franck-Condon region for a fixed orientation of the molecule. Madsen[15] studied the tunneling ionization rates and their angular dependence and confirmed the involvement of the same normal modes. Patchkovskii[14] studied the role of the dependence of the early time dynamics on the gradient and the curvature of the potentials in the vicinity of the T_d point on the large value of the ratio of the autocorrelation functions of CH_4^+ and CD_4^+.

We recently reported on the isotope effect that occurs in the methane cation when the neutral is photoionized by a XUV attopulse.[20] We carried out a fully quantum dynamical study in the three electronic states, using two nuclear coordinates described on a grid. The two coordinates span the normal modes of the molecule, with high weights on the two t_2 modes and the e mode involved in the JT distortion. The photoionization by the XUV attopulse was described by sudden ionization and the photoionization matrix elements are computed for each grid point geometry in the Franck-Condon region for an ensemble of 8000 orientations with respect to the electric field of the ionizing pulse. We considered two carrier frequencies of the pulse, which allows accessing the three lowest states of the cation in different amounts. A low carrier frequency ($\approx$13.65 eV) that corresponds to the 9th harmonic of a 800 nm IR pulse leads to populations in the ground state D_0 and the first excited state D_1 of the cation, with a very low amount in D_2. On the other hand, a carrier frequency that corresponds to the 11th harmonics (17.9 eV) accesses the three lowest states of the cation in roughly equal amounts. We showed by computing the ratio of the autocorrelation functions for an ensemble of randomly oriented molecules that a large isotope effect, with a ratio $\approx$ 2.6 at 1.6 fs, is obtained for a photoionization by the higher frequency $h\nu_{11}$ attopulse, that accesses the D_2 state. A lower isotope effect, with a ratio of 1.5 closer to the effective mass ratio (μ_{C-D}/μ_{C-H} =1.86), is obtained for

photoionization by the $h\nu_9$ attopulse, which does not significantly accesses the D_2 state. We further showed that the autocorrelation function of the initial state being an observable sensitive on electronic coherences, that the larger isotope effect has a quantum nature and is due to the short time dynamics of the electronic coherences that involve the D_2 state.

Here, we pursue our study of the role of electronic coherences in inducing large isotope effects, larger than the classical effect due to the different effective masses, by reporting fully quantal dynamical simulations following a sudden tunnelling ionizing effect, as is occurring in high harmonic spectroscopy. In order to assess the role of electronic coherences on the initial state that results from a tunneling ionization, we consider two field strengths of the IR pulse that generates the harmonics: a low strength of 0.03 a.u. (3.16 10^{13} W/cm^2) that does not significantly access the D_2 state in the Franck-Condon region and a larger field strength of 0.075 a.u. (2 10^{14} W/cm^2) that significantly accesses the D_2 state. Our results show that as in the photoionization case, a large isotope effect of ≈ 2.7 on the ratio of the autocorrelation functions is obtained for the stronger pulse, when the D_2 state is accessed.

We have previously reported similar isotope effects that arise when an electronic coherence reaches a region of non adiabatic coupling in the diatomic molecules N_2 and LiH.[21-23] We showed using algebraic techniques for one nuclear dimension that the direction and the magnitude of the amplitude transfer when the electronic coherence reaches the coupling region is governed by the phase difference between the two electronic states present in the wave packet. The phase difference factorizes into a classical term that depends linearly on the reduced mass and a purely quantum part, that is non linear in the mass.[24] The presence of this quantum term explains that the isotope effect is larger than the classical one when the vibronic wave packet is made of several electronic states.

We briefly report on the computational model in section 2, discuss the results for tunnel ionization in section 3 and provide a discussion of how the electronic coherences steer the isotope effect in section 4. Conclusions are given in Section 5.


2. Computational details

2.1 Electronic structure and nuclear grid

We use the same coordinates and the same level of electronic structure and the same potential energy surfaces (PES) as described in ref. [20]. The electronic structure is computed for the geometry of each grid point at the SA(3)-CASSCF (9,8) /6-31G++(2df,2pd) using MOLPRO,[25] which provides the values of the potential energy for the three states, D_0, D_1 and D_2 as well as

the non adiabatic couplings (NAC). The computed vertical IP at the T_d geometry is 13.6 eV. The results of the electronic structure are in good agreement with ref. [26]. The larger atomic basis set allows for a good description of the ionization process.

The three lowest states of the methane cation, D_0, D_1 and D_2, are unstable at the equilibrium geometry of the neutral ground state. The two nuclear coordinates of the grid, q_1 and q_2, are defined as linear combination of Cartesian displacements. They span the normal modes of the T_d geometry that are involved in the JT effect, as well as the seams between the electronic states in the Franck-Condon region, where the geometry is of lower symmetry. The potential energy surface (PES) of the ground state, D_0, exhibits two minima close to the FC region, the C_{2v} equilibrium geometry, and a secondary, less distorted, minimum of D_{2d} geometry ≈ 0.28 eV above the C_{2v} energy, see Figure 1. The coordinate q_1 points to the C_{2v} geometry and the coordinate q_2 to the D_{2d} one. To both, we added a small geometrical distortion in order to correctly describe the non adiabatic coupling (NAC) so that all geometries on the grid are of C_1 geometry. We include 146 point along q_1 and 184 along q_2, which leads to 26864 grid points per electronic state. Figure 1 shows isocontours of the PES of D_0, D_1 and D_2 for the q_1 and q_2 coordinates. In CH_4, the H nuclei are equivalent. For a particular realization as shown in the insets of Figure 1, without the distortions added to q_1 and q_2 that takes the geometries of the grid points out of the C_{2v} geometry, we should have two equivalent C_{2v} minima and a D_{2d}. The distortion, that is needed to capture the NAC seams, lowers the symmetry of one of the C_{2v} minima. On the grid, the geometry closest to the global C_{2v} minimum ($q_1=1.4$, $q_2=0$) has a root mean square deviation (RMSD) of 0.0418 Bohr. The D_{2d} minimum ($q_1=0$, $q_2=-1.12$, RMSD=0.0321 Bohr) is 0.165 eV higher than that of the C_{2v} one and the more distorted C_{2v} minimum ($q_1=1.08$, $q_2=1.26$, RMSD $= 0.1384$, closer to a C_s geometry) is 0.1583 eV higher than the C_{2v} minimum. D_1 exhibits three minima located close to the NAC seams while D_2 has a minimum at the T_d point. The PES's of the three states have very different gradients around the T_d point. The gradient of D_0 out of the unstable T_d point is very steep but the minima around D_{2d} and C_{2v} are very shallow. D_1 is also unstable at the T_d point, the D_1 PES exhibits three minima that are located close to the NAC seams with D_0. The PES around the T_d minimum on D_2 is very steep. This implies that the wave packet transferred to D_2 by the ionization process remains localized in this tight potential which makes the NAC with the D_1 and D_0 very efficient close to the T_d geometry. On the other hand, the initial wave packets on D_1 and D_0 rapidly leave the region of the unstable T_d geometry while the D_2 wave packet is trapped around the T_d point.
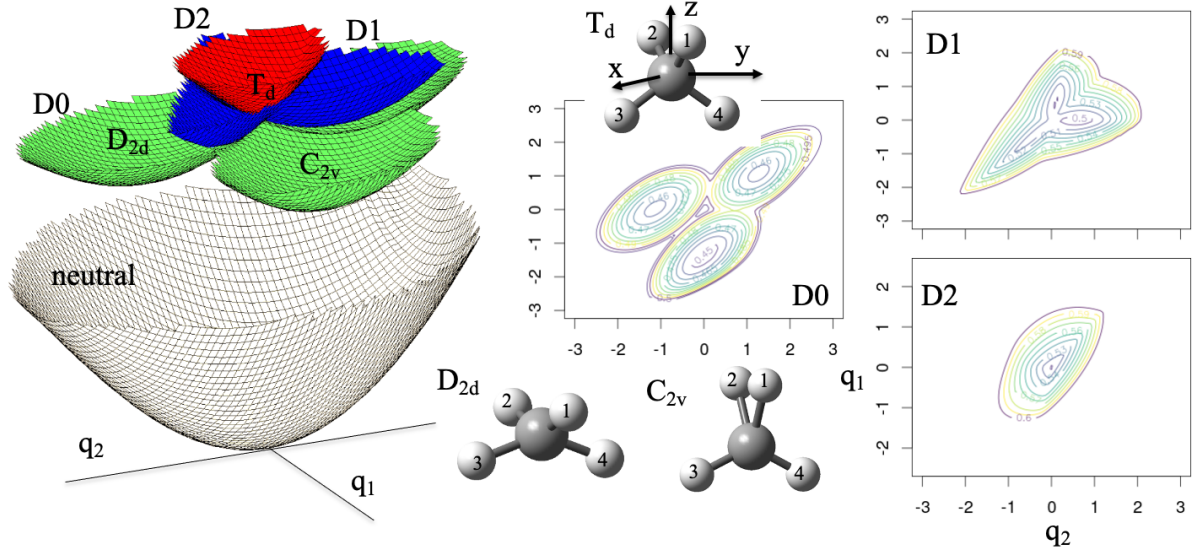
Figure 1: a) 3D view of the PES of the three lowest states of cation, D_0, D_1 and D_2, computed at the SA-3-(9,8) /6-31G++(2df,2pd). B: Isocontours of the PES, T_d geometry and geometries of the D_{2d} and C_{2v} minima on D_0. Isocontour spacing: D_0 0.01 eV D1. Isocontour spacing: 0.009 eV. C. D2. Isocontour spacing: 0.015 eV, and geometries on D_0.

2.2 Initial amplitudes in the states of the cation

The tunneling amplitudes on the three states of the cation are determined within the three step model,[27] assuming a tunneling ionization process at the maximum of the electric field for a random orientation of the molecular frame with respect to the laboratory frame. We use a MO-ADK model[28-29] for describing the tunneling ionization from the neutral ground state to a particular electronic state of the cation, D_i, and a given orientation of the electric field, $\hat{\mathbf{e}}_m$, with respect to the molecular frame at the nuclear geometry of a given grid point g. We further assume that the structure parameters that appear in the expression of the molecular asymptotic wave function closely resembles the one electron density of the active electron that is ionized.[30] The latter is given by the Dyson orbital, $\phi_{g,D_i}^{Dyson}(\mathbf{r}) = \int d\mathbf{r}_1...d\mathbf{r}_{N-1}\Psi_{g,D_i}^{cat}(\mathbf{r}_1..\mathbf{r}_{N-1})\Psi_{g,GS}^{neut}(\mathbf{r}_1,...,\mathbf{r}_N)$ with $\mathbf{r}$ the electronic coordinate and N the number of electrons of the neutral. The strong field ionization probabilities, W_{g,D_i}^m at each grid point to an electronic state of the cation D_i for a given orientation of the electric

field $\hat{\mathbf{e}}_m$ are then given as the product of the norm of the Dyson MO, $N_{g,D_i} = \int d\mathbf{r} \left| \phi_{D_i}^{Dyson}(\mathbf{r}) \right|^2$

multiplied by the Keldysh tunnel ionization rate,

$$K_{g,D_i}^m = \exp\left(-\frac{2}{3} \frac{\left(2 IP_{g,D_i}^m \right)^{3/2}}{|\mathbf{F}|} \right) \tag{1}$$

and weighted by the square modulus of the vibrational ground state wave function of the neutral

at this grid point, $\left| c_{g,GS}^{neut} \right|^2$ [31]

$$W_{g,D_i}^m = \left| c_{g,GS}^{neut} \right|^2 N_{g,D_i} K_{g,D_i}^m \tag{2}$$

In Eq.(1), $|\mathbf{F}|$ is the strength of the field. IP_{g,D_i}^m is the IP at the geometry of grid point g for a

given orientation of the electric field, $\hat{\mathbf{e}}_m$, corrected by the Stark shift due to the strong electric

field of the IR pulse on the neutral and on the cation.

$$IP_{g,D_i}^m = E_{g,D_i}^{cat} - E_{g,GS}^{neut} - |\mathbf{F}| \hat{\mathbf{e}}_m \cdot \left(\mu_{g,D_i}^{cat} - \mu_{g,GS}^{neut} \right) \tag{3}$$

where μ_{g,D_i}^{cat} and $\mu_{g,GS}^{neut}$ are the permanent dipoles of the cation state D_i and of the neutral at grid

point g. The Dyson MO's were computed as described in ref. [32] and their norm computed from

their expansion in AOs. At each grid point, the amplitudes of the initial state on each electronic

state of the cation are proportional to the ionization rates

$$c_{g,i}^m \propto \sqrt{W_{g,D_i}^m} \tag{4}$$

We show the localization of the initial state as a heatmap in the (q_1,q_2) coordinates in Figure 2

for CH_4^+ for two values of the field strength: a low value of 0.03 a.u. (3.16 10-13 W/cm^2),

called weak field (wf) in the following and a higher value of 0.075 a.u. (2 10^{14} W/cm^2), called

strong field (sf) in the following. This higher value corresponds to the peak power of the IR

800 nm pulse used to measure the high harmonic yields in ref. [12]. Each orientation $\hat{\mathbf{e}}_m$ defines

a pure state. In a typical experiment, the orientation of the molecule is random with respect to

the electric field. The results reported below are therefore computed for an ensemble of 8000

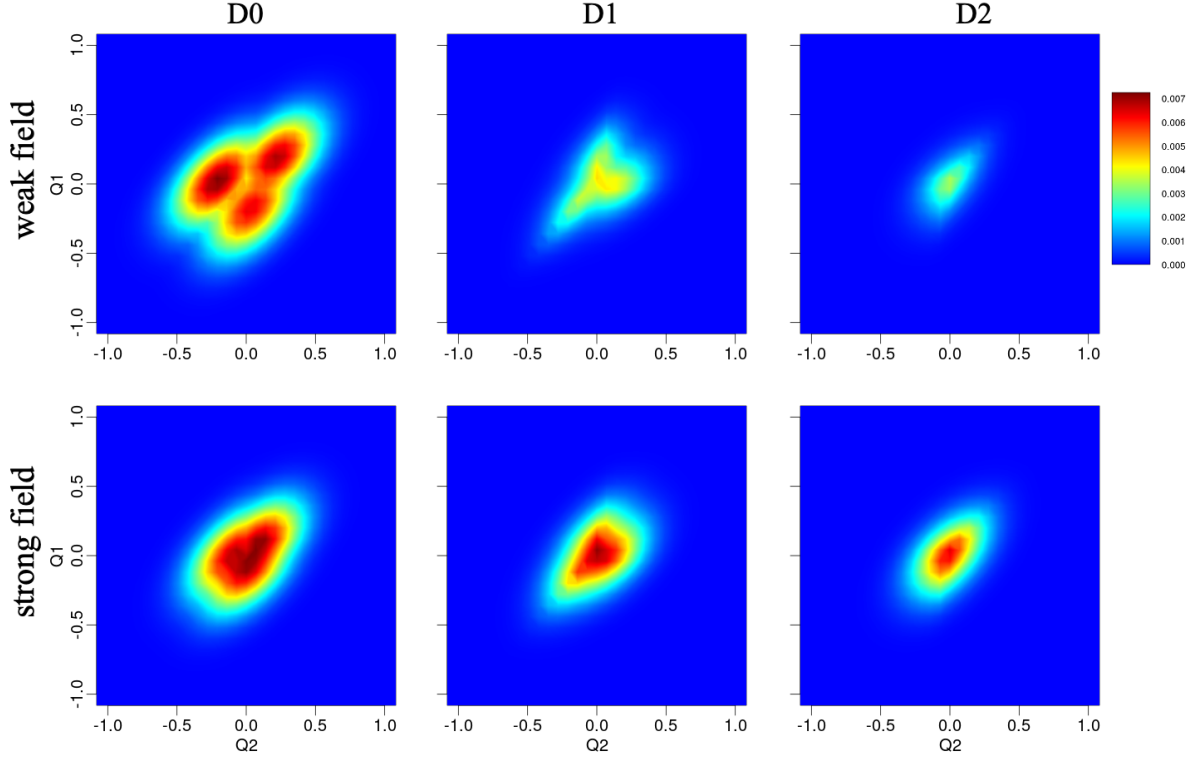random orientations on unit sphere.

Figure 2. Localization of the initial state, $\left|c_{gi}\right|^2 = \dfrac{1}{N} \displaystyle\sum_{m=1}^{8000} \left|c_{gi}^m\right|^2$ on the three electronic states,

D_0, D_1 and D_2 for CH_4^+ computed for an ensemble of 8000 random orientations on the unit sphere for the weak field strength, top row and the strong field strength, bottom row. The localization of the CD_4^+ initial states is shown in Figure S1.

The localization of the initial state on the three electronic states is shown in Figure 2 for the two field strengths for the methane cation CH_4^+. One can see that for the weak field, the localization of the initial state maps the isocontours of PES shown in Figure 1. The reason is that in the approximation we use, the dependence of the tunneling rate on the orientation comes from the Stark effect on the IP (Eq.(3)) which for this field strength is very weak. The tunneling rate then becomes determined by the field free energy difference between the neutral ground state and the electronic state of the cation at a given grid point. Since the PES of the neutral ground state is shallow in the Franck-Condon region, the variation of the IP on the grid is given by the energies of the cation states. The Stark effect is larger on the states of the cation than on the neutral GS. Therefore for higher field strengths, one obtains lower IP values than in the weak field case, which leads to a higher ionization yields, more initial populations in D_1 and D_2 and a more uniform localization of the initial states around the T_d point. We obtain very similar initial localization of the initial states for CD_4^+ see Figure S1 of the SI. The reason is

that the only isotopic dependence of the initial state comes from the localization of the ground vibrational state of the neutral on the grid. The latter is slightly more localized around the T_d geometry for CD_4^+ than for CH_4^+.

2.3 Vibronic Hamiltonian on the grid

On the grid, the vibronic Hamiltonian used to propagate the principal component vectors, $\mathbf{U_s}$, takes the form, see also Section S1 of the SI,

$$\mathbf{H}_{ig,jg'} = -\frac{1}{2}\mathbf{T}_{ig,jg'}\delta_{ij} + \mathbf{V}_{ig,jg}\delta_{ij}\delta_{gg'} + \left(\frac{1}{i}\tau_{ig,jg}\delta_{gg'}\right).\mathbf{P}_{igjg'} \tag{5}$$

The Hamiltonian includes the NAC coupling between each pair of electronic states. We neglect the second derivative NAC term which is much smaller. In the NAC term (last term of Eq. (5)), $i{\neq}j$.

In Eq. (5), the kinetic energy operator $\hat{T}$ in internal coordinates takes the form

$$\hat{T} = -\frac{1}{2}\left(\frac{1}{\mu_1}\frac{\hat{\partial}^2}{\partial q_1^2} + \frac{1}{\mu_2}\frac{\hat{\partial}^2}{\partial q_2^2} + \frac{2}{\mu_{12}}\frac{\hat{\partial}^2}{\partial q_1 \partial q_2}\right) \tag{6}$$

and the components of the non-adiabatic coupling vector, $\tau_{ig,jg}$, are expressed in internal coordinates. The derivation and the expression of the reduced masses is given in the SI, as well as 2D maps showing the value of two components of the NAC coupling vectors, $\tau_{ig,jg}\left(q_1\right)$ and $\tau_{ig,jg}\left(q_2\right)$ on the grid for the three pairs of states. $\mathbf{P}$ is the momentum vector, whose two components are given by $\frac{\hbar}{i}\frac{\partial}{\partial q_1}$ and $\frac{\hbar}{i}\frac{\partial}{\partial q_2}$. We solve the time-dependent Schrödinger equation, $i\hbar\frac{d\mathbf{c}}{dt} = \mathbf{Hc}$ numerically. The vector $\mathbf{c}$ is the vector of the complex amplitudes of the time-dependent wave function, $c_{ig}\left(t\right)$, on the grid. The non local kinetic energy and momentum matrix elements are computed using a finite difference algorithm, see SI. We report below the time-dependent value of the off diagonal term of the Hamiltonian averaged over grid points for each pair of electronic states:

$$H_{ij}(t) = \sum_g c_{ig}^{*}(t)\left(\frac{1}{i}\right)\tau_{ig,jg}\hat{P}\sum_{g'} c_{jg'}(t) \tag{7}$$

2.4 Quantum dynamics on the grid averaged over random orientations

We report below results of the quantum dynamics averaged over 8000 random orientations of the electric field with respect to the molecule. We performed the averaging as in ref. [20]. The initial density operator, $\hat{\rho}^{ens}(0)$, of the resulting ensemble is given by summing over the pure states defined by the M=8000 orientations

$$\hat{\rho}^{ens}(0) = \frac{1}{M}\sum_{m=1}^{M} |\Psi_m(0)\rangle\langle\Psi_m(0)| \tag{8}$$

The initial density matrix on the basis of the N_e =3 electronic states and N_g grid point can therefore be written as a quadratic form

$$\rho^{ens}(0) = \mathbf{A}\mathbf{A}^{\dagger} \tag{9}$$

where $\mathbf{A}$ is a rectangular matrix of dimensions (N_e x N_g = N_T) x M made of M column vectors for each sampled orientation, $\mathbf{c}_m$, of N_T c_{ig}^m complex amplitudes. Since we compute N_g=26864 grid points per electronic state, N_T >>> M. We showed in ref.[20] that one can find the principal components of the matrix rectangular $\mathbf{A}$ by singular value decomposition:

$$\mathbf{A} = \mathbf{U}\mathbf{\Sigma}\mathbf{V}^{\dagger} \tag{10}$$

The matrix $\mathbf{\Sigma}$ is the diagonal matrix of the M non zero eigenvalues of $\mathbf{A}$. $\mathbf{U}$ is a N_T x M matrix whose columns are the left eigenvectors of $\mathbf{A}$ that correspond to a non zero eigenvalues. The MxM matrix $\mathbf{V}$ is the matrix whose columns correspond to the M right eigenvectors of $\mathbf{A}$. One also shows that the matrix $\rho^{ens}(0)$ is rank deficient and has at most M non zero eigenvalues with eigenvectors given by $\mathbf{U_s}$. We can therefore exactly rewrite $\rho^{ens}(0)$ is a sum of M 'pure states' which are its principal components:

$$\rho^{ens}(0) = \mathbf{U}\mathbf{\Sigma}\mathbf{V}^{\dagger}\mathbf{V}\mathbf{\Sigma}\mathbf{U}^{\dagger} = \mathbf{U}\mathbf{\Sigma}^2\mathbf{U}^{\dagger} = \sum_{s=1}^{M} \omega_s^2 \mathbf{U}_s\mathbf{U}_s^{\dagger} \tag{11}$$

To compute the average dynamics, it is therefore strictly equivalent to solve the time-dependent Schrödinger equation for the M $\mathbf{U_s}$ vectors or for the M: $\mathbf{c_m}$ ones. However, if the $\mathbf{A}$ matrix has a number of eigenvalues L that are much larger than the rest of them, we can approximately write its expansion (Eq. (11)) in terms of L principal components $\mathbf{U_s}$, $L << M$:

$$\rho^{ens}(0) \approx \sum_{s=1}^{L} \omega_s^2 \mathbf{U}_S \mathbf{U}_S^\dagger, \, L << M \tag{12}$$

In that case, propagating the L principal components leads to a considerable saving of computer time. In ref.[20], we could show analytically that for initial states produced by sudden ionization, there were exactly $L=3$ principal components of $\mathbf{A}$. In the case of initial amplitudes resulting from a sudden tunneling ionization process, we do not have such an analytical result because analytical dependence of the Keldysh tunneling ionization rates on the orientation of the field, see Eq. (1). However, the dynamics of the ensemble is recovered by three principal components which capture 99.97 % of the trace of the ensemble density matrix for either one of the two isotopomers and for either of the two field strengths. More details are given in the SI.

We propagate the time-dependent Schrödinger equation using a finite difference algorithm for the kinetic energy and momentum operators for the three initial $\mathbf{U_s}$ vectors. The probabilities for each initial state at each grid point are given by

$$P_{ig}(t) = \rho_{ig,ig}^{ens}(t) = \sum_{s=1}^{L} w_s \left| u_{ig}^s(t) \right|^2 \tag{13}$$

where $u_{ig}^s(t)$ are the components of $\mathbf{U_s}(t)$ on the basis set and $w_s = \omega_s^2 / \mathrm{Tr}\left[\rho(0)\right]$. The coherences terms of the ensemble density matrix take the form

$$\rho_{ig,jg'}^{ens}(t) = \sum_{s=1}^{L} w_s u_{ig}^s(t) u_{jg'}^s(t) = \sum_{s=1}^{L} w_s \rho_{ig,jg'}^s(t) \tag{14}$$

where $\hat{\rho}^s(t) = \left| U_S \right\rangle \left\langle U_S \right|$ is the density matrix corresponding to its principal vector eigenvector $\mathbf{U_s}$.

The localization of the electronic coherence between electronic state i and j is diagonal in the grid index :

$$\rho_{ig,jg}^{ens}(t) = \sum_{s=1}^{L} w_s u_{ig}^s(t) u_{jg}^s(t) = \sum_{s=1}^{L} w_s \rho_{ig,jg}^s(t) \qquad i \neq j \qquad (15)$$

We report in the figures below the electronic coherences summed over all grid points

$$\rho_{ij}^{ens}(t) = \sum_{g}^{N_g} \sum_{s=1}^{L} w_s u_{ig}^s(t) u_{jg}^s(t) = \sum_{g}^{N_g} \sum_{s=1}^{L} w_s \rho_{ig,jg}^s(t), \quad i \neq j \qquad (16)$$

The square modulus of the autocorrelation of the initial state takes the form:

$$\left| C(t) \right|^2 = \mathrm{Tr}\left[\rho^{ens}(0) \rho^{ens}(t) \right] =$$

$$\sum_{ig} \langle ig | \sum_s w_s | u_s(0) \rangle \langle u_s(0) | \sum_{jg'} | jg' \rangle \langle jg' | \sum_{s'} w_{s'} | u_{s'}(t) \rangle \langle u_s'(t) | ig \rangle$$

$$= \sum_{ig} \sum_{jg'} \sum_s w_s u_{ig}^s(0) u_{jg'}^s(0)* \sum_{s'} w_{s'}(0) u_{jg'}^{s'}(t) u_{ig}^{s'}*(t)$$

$$= \sum_{ig} \sum_{jg'} \left(\sum_s w_s \rho_{ig,jg'}^s(0) \right) \left(\sum_{s'} w_{s'} \rho_{jg',ig}^{s'}(t) \right)$$

$$(17)$$

So using Eq. (14), we see that

$$\left| C(t) \right|^2 = \mathrm{Tr}\left[\rho^{ens}(0) \rho^{ens}(t) \right] = \sum_{ig} \sum_{jg'} \rho_{ig,jg'}^{ens}(0) \rho_{ig,jg'}^{ens\,*}(t)$$

$$= \sum_{ig} \rho_{ig,ig}^{ens}(0) \rho_{ig,ig}^{ens\,*}(t) + \sum_{i} \sum_{g' \neq g} \rho_{ig,ig'}^{ens}(0) \rho_{ig,ig'}^{ens\,*}(t) + \sum_{i \neq j} \sum_{g',g} \rho_{ig,jg'}^{ens}(0) \rho_{ig,jg'}^{ens\,*}(t)$$

$$(18)$$

is a direct probe of the electronic coherences (last term in Eq. (18)). The second term corresponds to vibrational coherences on the same electronic state. Since the yield in harmonics is proportional to $\left| C(t) \right|^2$,[19] the harmonic yield is an experimental probe of electronic coherences.

3. Results and discussion

3.1 Population and electronic coherences dynamics on the nuclear time scale

The time evolution of the probabilities of each electronic state, $P_i(t) = \sum_{g=1}^{N_g} P_{ig}(t)$, was

computed using Eq. (13) for tunneling initial states resulting from tunnel ionization by the weak field (Figure 3a) and by the strong field pulse (Figure 3b) for the two isotopomers.
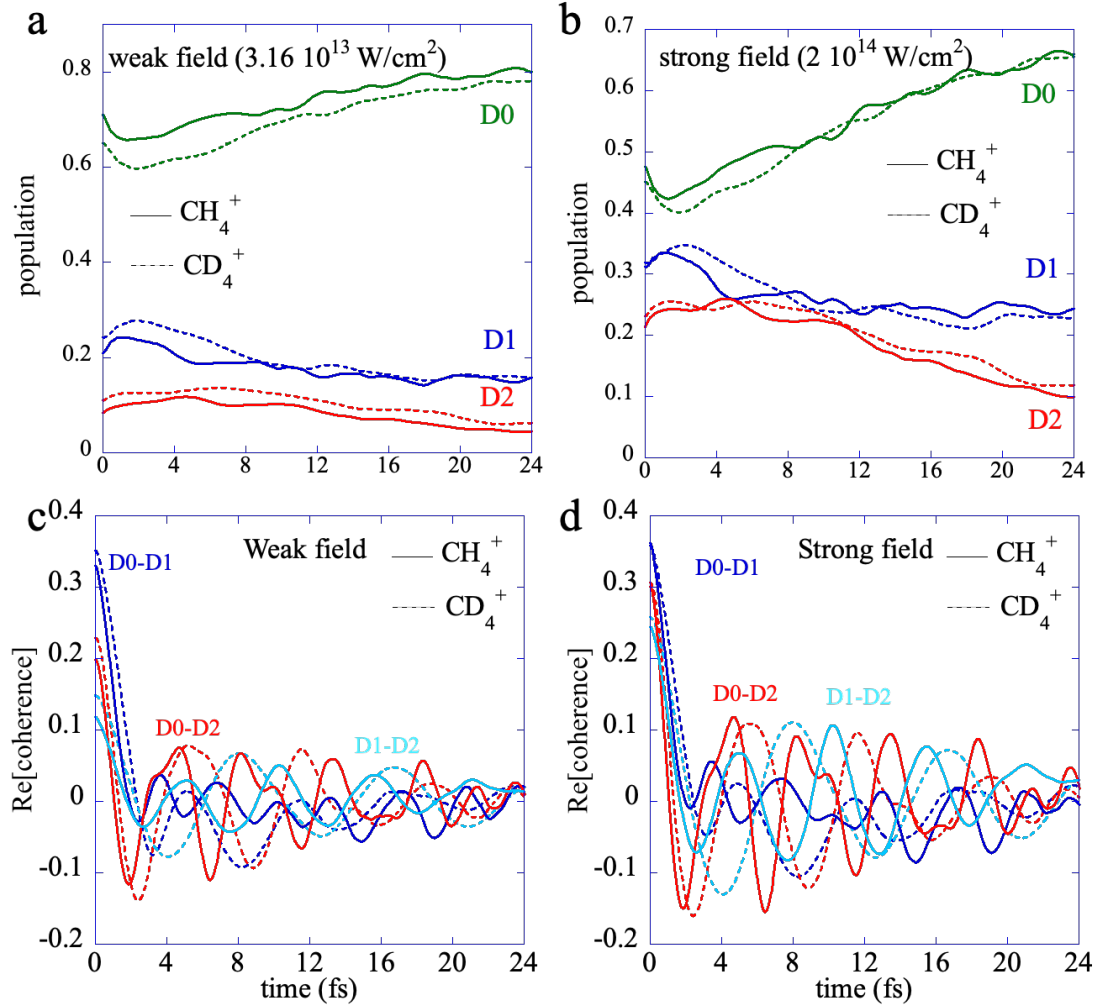
Figure 3. Panels a and b: Population dynamics, $P_i(t)$, for the ensemble of CH_4^+ (full lines) cations and CD_4^+ (dotted lines) upon tunneling ionization by a weak field (a) and a strong field (b). The population in D_0 is plotted in green, in D_1 in blue and in D_2 in red. Panels c and d: Electronic coherence dynamics (Eq. (16)): c - weak field, d - strong field. The D_0-D_2 electronic coherence is plotted in red, the D_0-D_1 one in blue, and the D_1-D_2 coherence in azure.

One can see from Figure 3 that the weak field strength (0.03 a.u., 3.16 10^{13} W/cm^2) pulse preferentially ionizes the ground state D_0 (initial populations on D_0 are 0.71 for CH_4^+ and 0.65 for CD_4^+). The initial population in D_1 is 0.21 for CH_4^+ and 0.24 for CD_4^+, about the double of that of D_2 (0.08 for CH_4^+ and 0.11 for CD_4^+). On the other hand, as discussed in section 2.3 above, the populations in D_1 and D_2 are larger for a tunnel ionization with the stronger pulse of 0.075 a.u. (2 10^{14} W/cm^2): 0.31 for CH_4^+ and 0.32 for CD_4^+ in D_1, 0.21 for CH_4^+ and 0.23 for CD_4^+ in D_2 and 0.48 for CH_4^+ and 0.45 for CD_4^+ for D_0. The tunneling ionization process creates a superposition of states for each orientation of the electric field which leads to electronic coherences at the level of the ensemble. The electronic coherences summed over all grid points, Eq. (16), are plotted in panels c and d of Figure 3. The oscillations in the populations are due to the non adiabatic transfers that are driven by the nuclear motion. One can see that the maximum of the oscillations of the population transfer coincide with large amplitudes of the oscillations of the electronic coherences. This is particularly clear at short time and for the oscillations of the D_0-D_2 electronic coherence. One also notices that oscillations of the electronic coherences in CD_4^+ are slower than in CH_4^+ and have a larger amplitude for the strong field initial states because there are more initial populations in the D_2 and the D_1 states. The oscillations of the electronic coherences are not periodic because of the strong NAC between the electronic states and the fact that the energy difference between the adiabatic electronic states varies rapidly in the FC region, see Figure 1. The coherences between the D_2 and the two lower states D_0 and D_1 are sustained by the NAC as long as there is population in the D_2 state because the latter is trapped around the T_d point on the steep D_2 potential. On the other hand, the wave packets on D_1 and D_0 are moving faster out of the T_d region because of the steep gradient of the PES around T_d.

3.2 Population and electronic coherences dynamics on the electronic time scale

The short time behavior up to 2 fs of the populations in the three electronic states and the electronic coherences (Eq. (16)) are shown in Figure 4 for the weak field (Fig. 4a) and the strong field (Fig.4b) initial states and the two isotopomers. Even on the short time (1.6 fs) probed by high harmonic spectroscopy using an 800 nm IR pulse,[12-13] the populations in each electronic state start to vary since the initial state of the cation is localized around the T_d point, where there is a strong non adiabatic coupling. The isotope effect on the populations is not very large. On the other hand, the periods of the oscillations of the electronic coherences are strongly affected by the isotopic substitution as shown in Figure 4c for the weak field initial state and

in Figure 4d for the strong one. On can see as expected that the dynamics of the D_0-D_1 coherence is not very much affected by the initial state while that of D_0-D_2 and D_1-D_2 coherence differ more because in the strong field case there is a larger amount of population initially present in D_2.

We compare in Figures 4e and 4f the time evolution of the electronic coherences for weak and strong field for CH_4^+ and CD_4^+ respectively. The onset of the differences in the dynamics of the electronic coherences occurs earlier for CH_4^+ than for CD_4^+. In this short time range, the nuclei have hardly time to move. We show in section 4 below that the difference is mainly due to the difference in the magnitude of amplitude transfers due to the non adiabatic couplings, in particular for the D_1-D_2 electronic coherence. The longer time dynamics is shown in Figure S2. One can see that the oscillations of the electronic coherences are getting slightly out of phase for the two field strengths as the dynamics unfolds, which is a manifestation of the effect of the amplitude transfers due to the NAC that involve the D_2 state. This effect is larger for CH_4^+ than for CD_4^+.
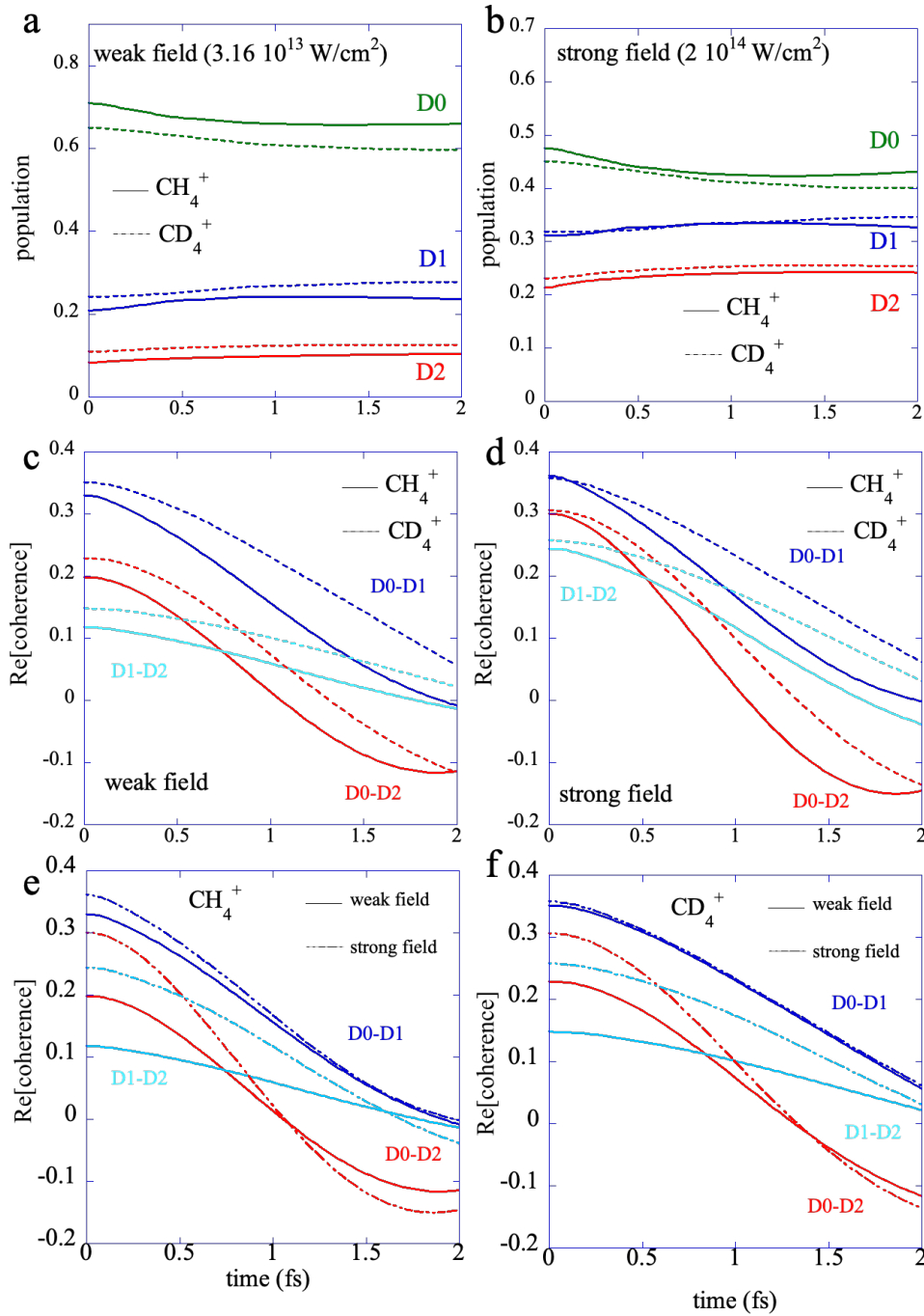
Figure 4. Panels a, b, c, d: same as Figure 3 for the short time range 0 to 2fs . One can see that the D_0-D_1 coherence is not much affected by the localization of the initial state and the initial population in the D_2 state while the D_2-D_0 and D_1-D_2 coherences are very much affected. Panels e and f: Comparison of the time evolution of the electronic coherences at weak and strong field for CH_4^+ (e) and CD_4^+ (f). Here too, the biggest differences are for the D_2-D_0 and D_1-D_2 coherences.

17

We next show in Figure 5a the auto correlation functions (Eq. (17)) and their ratio (Figure 5b) for the four cases. We obtain a ratio of the autocorrelation functions, $\left|C(t)\right|_D^2 \Big/ \left|C(t)\right|_H^2$ at 1.6 fs equal 2.4, in very good agreement with ref. [12] for the high field strength initial state, and of 1.6 for lower field strength one. The large ratio of 2.4 computed for the high field strength initial state is due to the interplay between the electronic coherences that involve the D_2 state and the onset of nonadiabatic interactions as the nuclei start to move. On the other hand, the ratio $\left|C(t)\right|_D^2 \Big/ \left|C(t)\right|_H^2 = 1.6$ is essentially due to the isotope effect due to the D_0-D_1 coherence. This value is smaller but close to the ratio of 1.86 that one expects on the basis of the ratio of the effective masses of the C-D and C-H bonds. When the terms that involve the electronic coherences D_2-D_0 and D_2-D_1 in the last term of Eq. (18) are not included in the computation of the autocorrelation functions, dotted lines in Fig. 5b, the ratio $\left|C(t)\right|_D^2 \Big/ \left|C(t)\right|_H^2$ is similar for the high and low field initial states (equal $\approx$ 1.6 to strong field and 1.4 for weak field). The effect of the NAC is further seen by comparing Fig5a and 5c with Fig.5b and 5d which are computed without including the NAC term in the Hamiltonian, Eq. (5). In that case, the ratio for strong and weak field initial states is $\approx$ 1.3 and it is 1.15 when the coherence terms due to the D_2 are not included in the dynamics.
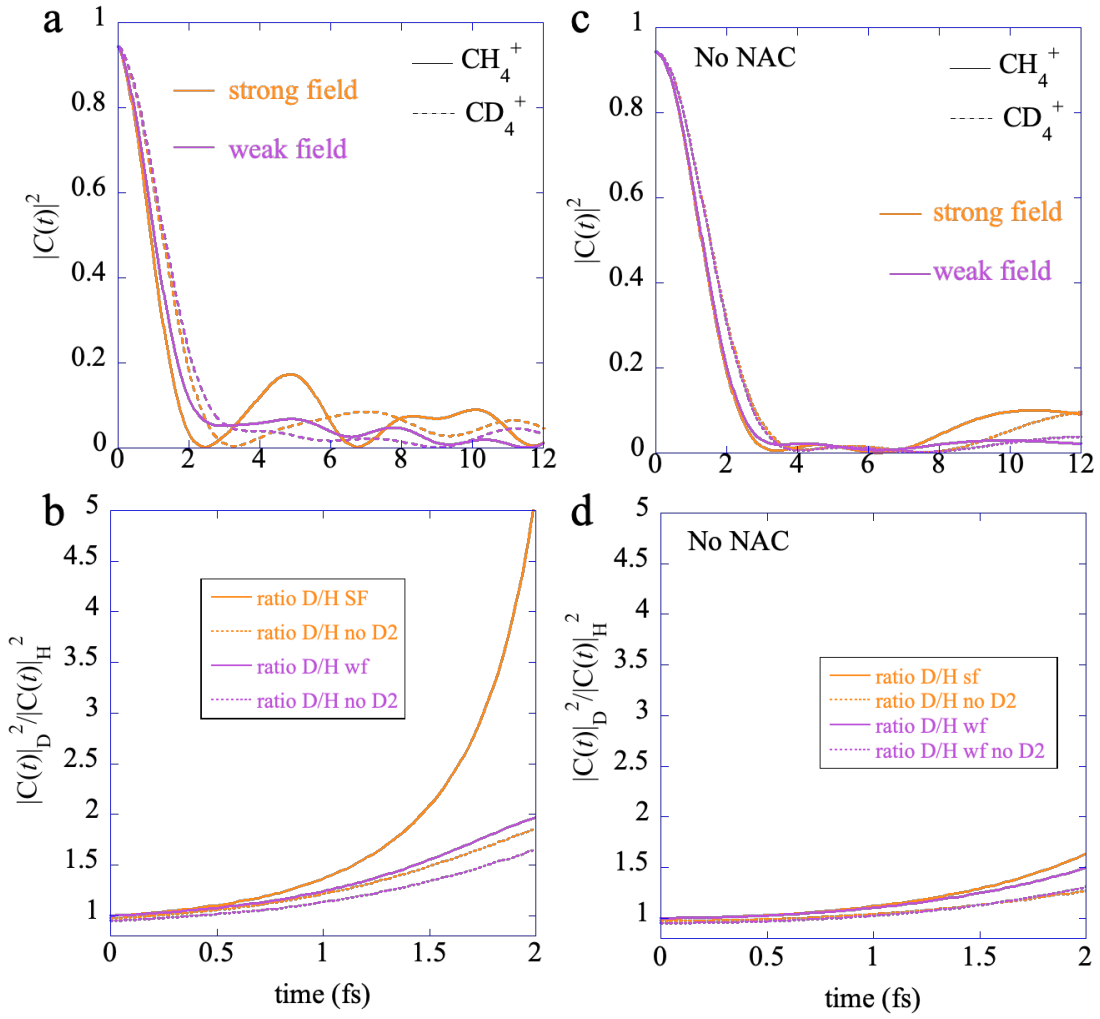
Figure 5.a) Autocorrelation functions, $\left|C(t)\right|^2$ (Eq. (17), of the weak field, (violet) and strong field (orange) initial states for CH_4^+ (full lines) and CD_4^+ (dashes) b) Ratio of the autocorrelation functions, $\left|C(t)\right|_D^2 \Big/ \left|C(t)\right|_H^2$, computed exactly (full lines) and without included the coherent terms involving the D_2 states (dots) c) Autocorrelation functions of the initial state without including the NAC in the Hamiltonian for computing the dynamics d) Ratio of the autocorrelation functions computed without NAC in the Hamiltonian.

4 Discussion

The results presented in section 3 point to a dominant role of the interplay between the electronic coherences and the non adiabatic coupling in getting an isotope effect different from that expected in the basis of the effective mass ratios. Indeed, the computed ratio of the masses in the kinetic energy term and in the NAC term in the Hamiltonian are ≈ 2. The heat maps of the localization of the two components of the NAC vectors (Eq. S6), $\tau_{ij}(q_1)$ and $\tau_{ij}(q_2)$, at each grid point are plotted in Figures S3-S4 for CH_4+ and Figure S5 for CD_4+. In the Franck-Condon region of the initial state population the seams of the NAC exhibit different localization for the D_0-D_1 and D_1-D_2 coupling (Figures S4-S5). The D_0-D_2 NAC values on the grid are 50 times smaller than those of D_0-D_1 and D_1-D_2. The D_0-D_1 coupling is localized towards the positive values of the (q_1, q_2) coordinates, while D_1-D_2 are primarily coupled towards the negative values of the (q_1, q_2). This results in the population flow that is localized at specific zones in phase-space and it is responsible for the rapid reorganization of the population in all three electronic states (movies S1-S4 in the SI).

We show in Figure 6 heatmaps of the spatial localization of the electronic coherences in coordinate space and in Figure 7 in momentum, computed for the D_0-D_1 and D_1-D_2 electronic coherences, top row CH_4^+, middle row CD_4^+ and bottom row CH_4^+ without including the NAC term in the Hamiltonian. The patterns that develop as a function of time follow the patterns of the localization of the components of the NAC vector shown in Figure S6. They are slower to develop for CD_4^+ than for CH_4^+ as already seen in Figure 4. In the bottom row of Figure 6, computed for CH_4^+ without including the NAC term, one sees that the localization of the electronic coherences hardly changes during the first 2 fs because the wave packets have hardly moved. This can be verified from the movies of the localization of the wave packets on D_0, D_1 and D_2 computed with and without NAC for the two isotopomers (see SI).
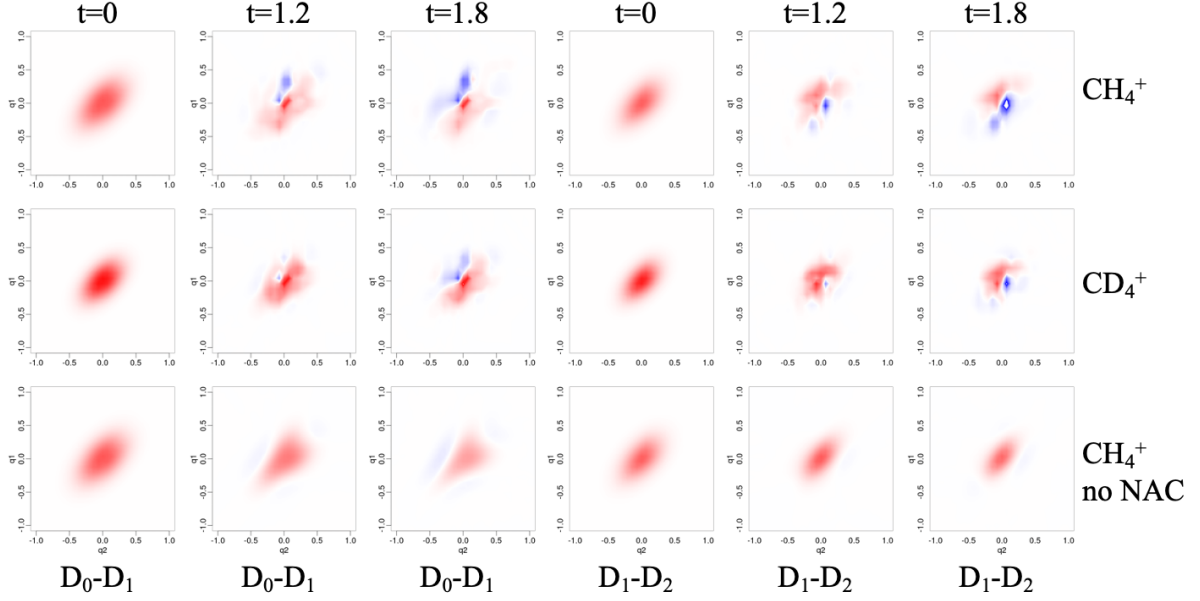
Figure 6: Heatmaps of the dynamics of the localization of the real part of electronic coherences, D_0-D_1 and D_2-D_1 at every grid point for the strong field case, computed for CH_4^+ (top row), CHD_4^+ (middle row) and CH_4^+ without including the NAC term in the Hamiltonian (bottom row). The time is in fs.
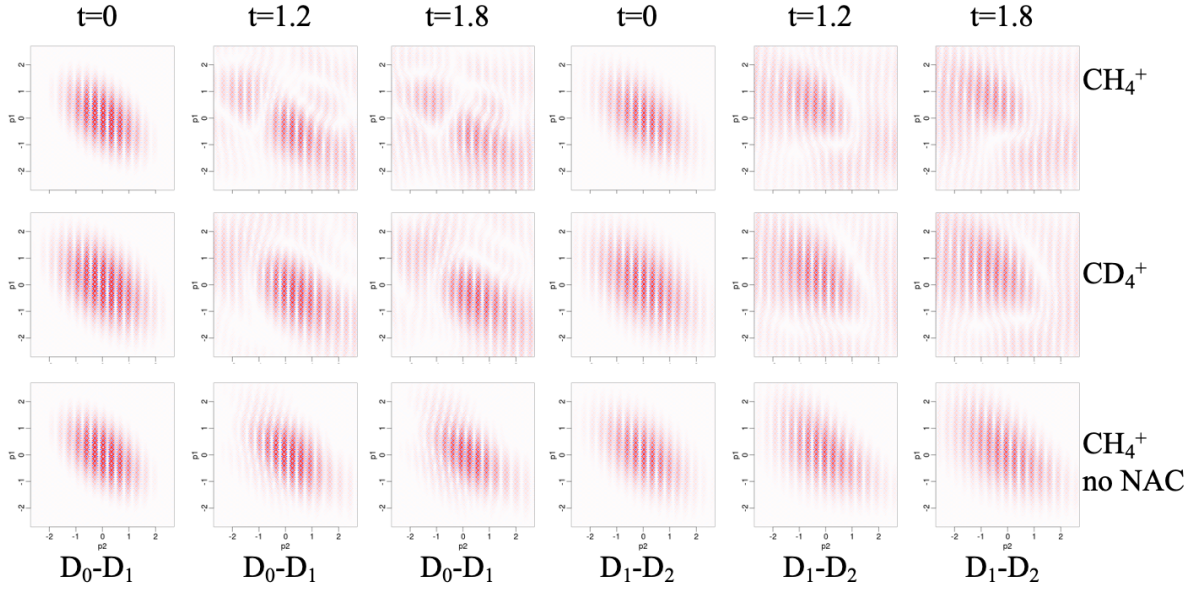

Figure 7: Heatmaps of the dynamics of the localization of the real part of electronic coherences, D_0-D_1 and D_2-D_1 in momentum space for the strong field case, computed for CH_4^+ (top row), CHD_4^+ (middle row) and CH_4^+ without including the NAC term in the Hamiltonian(bottom row).

21

We show in Figure 7 the localization of the electronic coherences in momentum space. The fast oscillations in momentum are due to the overall size of the coherence in space and they are slightly slower for CD_4^+ than for CH_4^+. The development of smaller patterns in the momentum coherence maps results from the fragmentation of the electronic coherences due to the NAC term in the Hamiltonian.

The development of patterns of the electronic coherences in space and in momentum before the nuclei start to move is a manifestation of a purely electronic time scale due to the NAC coupling. They result from the interplay between the localization in space of the NAC seams shown in Figure S6 and the momentum term of the Hamiltonian, see Eq. (5). Since the NAC terms exhibit the expected ratio of ≈ 2 at every grid point, the strong non classical isotope effect in the ratio of the autocorrelation functions plotted in Figure 5 arises from the momentum term. It is due to the fact that the tunneling ionization process creates a coherent superposition of the states of the cation. When the NAC term acts on an already existing coherence between the two states that are coupled, the direction and the magnitude of the amplitude transfer depend on the phase of the electronic coherence. We showed in refs.[22-23] for diatomic molecules using a Condon approximation[33] for the non adiabatic coupling that the transfer is maximum when the phase the momentum overlap between the wave packet on each coupled electronic state, $\langle i | \hat{P} | j \rangle$, is stationary. On the grid, we have an exact Condon-like separation at each grid point, see Eq. (5). The value of the NAC coupling, $H_{ij}(t)$, averaged over grid points between the wave packets on the two states that are coupled as a function of time is given by Eq. (7). Only the phases of the D_1-D_2 and D_0-D_1 coherences become stationary between 1 and 2 fs, and this only for the q_2 components of the NAC vector τ_{ij}. The values of the phase and the modulus of $H_{ij}(t)$ are plotted in Figure 8a for the weak field case and in Figure 8b for the strong field case. The plots for the other coherences are given in Figure S6 of the SI. Movies of the rates of population transfer for the strong field initial state at each grid points are available in the SI. One can see from Figure 8 that the phases become stationary at earlier times for CH_4^+ than for CD_4^+ which explains the earlier onset of amplitude transfer for CH_4^+ between these two pairs of states. One also see that the modulus of the coupling term is significantly larger for the D_1-D_2 coherence for strong field initial state, which explains the important role played by this coherence in the non classical strong isotope effect observed on the ratio of the autocorrelation

functions in that case. Conversely, in the weak field case, one is getting an isotope effect smaller than expected on the mass ratio, which is essentially due to the D_0-D_1 electronic coherence. We note also that at short time, it is the component of the NAC vector along q_2 that is pointing to the secondary D_{2d} minimum that is dominant in the amplitude transfer.
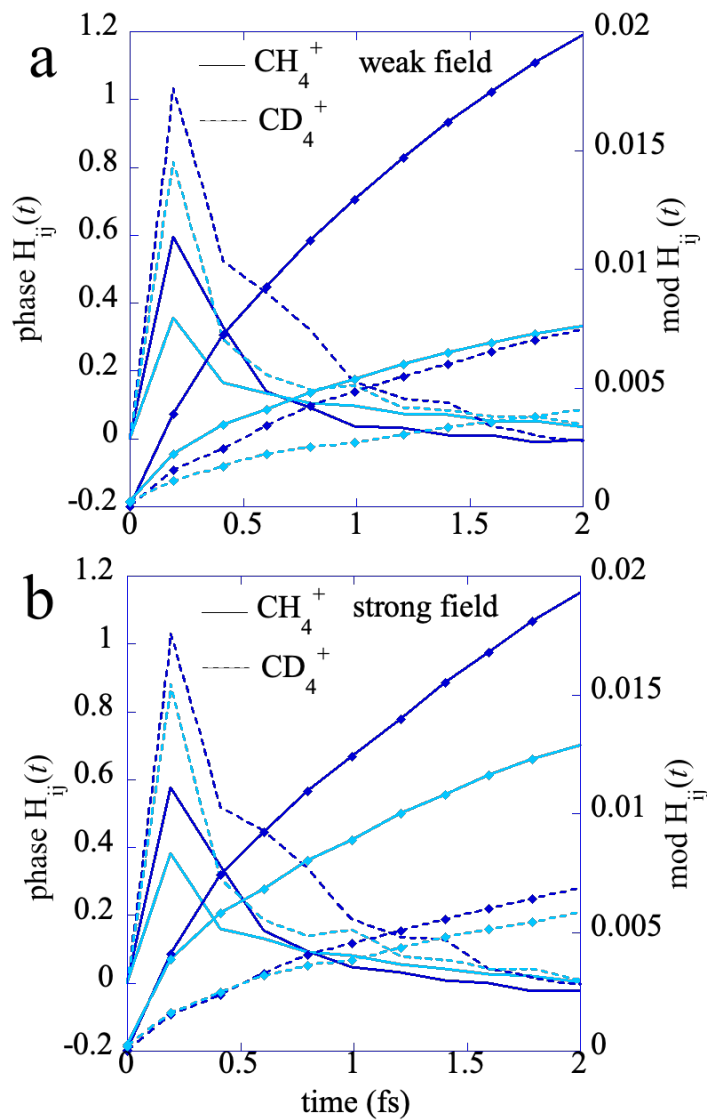

Figure 8. Early time evolution of the phases (left y axis) and moduli (right y axis) of NAC term $H_{ij}(t)$, Eq. (7), computed for the q_2 component of the NAC vector for the weak field (panel a) and strong field (panel b) initial states for the two isotopomers (CH_4^+ in full lines and CD_4^+

in dashes). The moduli are plotted with diamonds symbols. The D_0-D_1 electronic coherence term is plotted in blue and the D_1-D_2 one in azure.

5. Conclusions

We investigated the very early time dynamics of the two isotopomers of the methane cation obtained by strong field ionization of the neutral ground state. We showed that the tunneling ionization prepares a superposition of the three lowest states of the cation. Two field strengths were considered, a weaker field that effectively does not access the higher D_2 electronic state and a stronger one for which the D_2 is significantly populated. The prompt electronic dynamics that follows the strong field ionization process exhibits a strong isotope dependence with a ratio of 2.4 in the autocorrelation functions, in agreement with the high harmonic spectroscopy experimental results which involve a tunneling ionization process.[12-13] On the other hand, the dynamics for the weak field initial state leads to an isotope effect of 1.4 in the autocorrelation functions, which is smaller than the mass ratio. The magnitude of the effect is not changing upon averaging over the orientation of the electric field of the ionizing pulse with respect to the molecule. For both cases, we show that the isotope effect has a non classical origin and is due to the interplay between the dynamics of the electronic coherences and the amplitude transfers between each pair of electronic states due to the non adiabatic coupling. This non classical isotope effect occurs on a purely electronic time scale, before a significant onset of nuclear motion. We generalized the analysis of the isotope effect for systems in a coherent superposition of states developed for diatomic molecules[21-24] to the present case of a 2D system, for which the NAC seams exhibit complex localization in space. We show by analyzing the phase and the modulus of the non adiabatic coupling between each pair of states that the D_0-D_1 and the D_1-D_2 electronic coherences play a major role in the non classical isotope effect. These are the coherences for which the phase of the coupling term, becomes stationary, which is the condition for an efficient amplitude transfer.

References

1.Corkum, P. B.; Krausz, F., Attosecond Science. *Nat. Phys.* **2007**, *3*, 381-387.

2.Krausz, F.; Ivanov, M., Attosecond Physics. *Rev. Mod. Phys.* **2009**, *81*, 163-234.

3.Goulielmakis, E., et al., Single-Cycle Nonlinear Optics. *Science* **2008**, *320*, 1614-1617.

4.Calegari, F.; Sansone, G.; Stagira, S.; Vozzi, C.; Nisoli, M., Advances in Attosecond Science. *J. Phys. B* **2016**, *49*, 062001.

5.Galli, M., et al., Generation of Deep Ultraviolet Sub-2-Fs Pulses. *Opt. Lett.* **2019**, *44*, 1308-1311.

6.Hernández-García, C.; Popmintchev, T.; Murnane, M. M.; Kapteyn, H. C.; Plaja, L.; Becker, A.; Jaron-Becker, A., Isolated Broadband Attosecond Pulse Generation with near- and Mid-Infrared Driver Pulses Via Time-Gated Phase Matching. *Opt. Express* **2017**, *25*, 11855-11866.

7.Nisoli, M.; Decleva, P.; Calegari, F.; Palacios, A.; Martín, F., Attosecond Electron Dynamics in Molecules. *Chem. Rev.* **2017**, *117*, 10760-10825.

8.Lepine, F.; Ivanov, M. Y.; Vrakking, M. J. J., Attosecond Molecular Dynamics: Fact or Fiction? *Nat Photon* **2014**, *8*, 195-204.

9.Vrakking, M. J. J.; Lepine, F., *Attosecond Molecular Dynamics*. The Royal Society of Chemistry: Cambridge, 2019; p P001-500.

10.Remacle, F.; Levine, R. D., An Electronic Time Scale for Chemistry. *Proc. Natl. Acad. Sci. USA* **2006**, *103*, 6793-6798.

11.Muskatel, H. B.; Remacle, F.; Levine, R. D., The Post Born-Oppenheimer Regime: Dynamics of Electronic Motion in Molecules by Attosecond Few Cycle Spectroscopy. *Phys. Scri.* **2009**, *80*, 048101-7.

12.Baker, S.; Robinson, J. S.; Haworth, C. A.; Teng, H.; Smith, R. A.; Chirilă, C. C.; Lein, M.; Tisch, J. W. G.; Marangos, J. P., Probing Proton Dynamics in Molecules on an Attosecond Time Scale. *Science* **2006**, *312*, 424.

13.Marangos, J. P.; Baker, S.; Kajumba, N.; Robinson, J. S.; Tisch, J. W. G.; Torres, R., Dynamic Imaging of Molecules Using High Order Harmonic Generation. *Phys. Chem. Chem. Phys.* **2008**, *10*, 35-48.

14.Patchkovskii, S., Nuclear Dynamics in Polyatomic Molecules and High-Order Harmonic Generation. *Phys. Rev. Lett.* **2009**, *102*, 253602.

15.Madsen, C. B.; Abu-samha, M.; Madsen, L. B., High-Order Harmonic Generation from Polyatomic Molecules Including Nuclear Motion and a Nuclear Modes Analysis. *Phys. Rev. A* **2010**, *81*, 043413.

16.Mondal, T.; Varandas, A. J. C., The Jahn-Teller Effect in the Triply Degenerate Electronic State of Methane Radical Cation. *J. Chem. Phys.* **2011**, *135*, 174304.

17.Mondal, T.; Varandas, A. J. C., On Extracting Subfemtosecond Data from Femtosecond Quantum Dynamics Calculations: The Methane Cation. *J. Chem. Theory Comput.* **2014**, *10*, 3606-3616.

18.Mondal, T.; Varandas, A. J. C., Structural Evolution of the Methane Cation in Subfemtosecond Photodynamics. *J. Chem. Phys.* **2015**, *143*, 014304.

19.Lein, M., Attosecond Probing of Vibrational Dynamics with High-Harmonic Generation. *Phys. Rev. Lett.* **2005**, *94*, 053004.

20.Gonçalves, C. E. M.; Levine, R. D.; Remacle, F., Ultrafast Geometrical Reorganization of a Methane Cation Upon Sudden Ionization: An Isotope Effect on Electronic Non-Equilibrium Quantum Dynamics. *Phys. Chem. Chem. Phys.* **2021**, *23*, 12051-12059.

21. Ajay, J. S.; Komarova, K. G.; Remacle, F.; Levine, R. D., Time-Dependent View of an Isotope Effect in Electron-Nuclear Nonequilibrium Dynamics with Applications to N2. *Proc. Natl. Acad. Sci. U.S.A* **2018**, *115*, 5890-5895.

22. Komarova, K.; vandenWildenberg, S.; Remacle, F.; Levine, R. D., Correlated Electron-Nuclear Motion During Non-Adiabatic Transitions in Lih and Its Isotopomers. *J. Phys. B* **2020**, *53*, 134001.

23. Komarova, K. G.; Remacle, F.; Levine, R. D., Time Resolved Mechanism of the Isotope Selectivity in the Ultrafast Light Induced Dissociation in N2. *J. Chem. Phys.* **2019**, *151*, 114308.

24. Komarova, K.; Remacle, F.; Levine, R. D., The Density Matrix Via Few Dominant Observables: The Quantum Interference in the Isotope Effect for Atto-Pumped N2. *J. Chem. Phys.* **2021**, *155*, 024109.

25. Werner, H.-J.; Knowles, P. J.; Knizia, G.; Manby, F. R.; Schütz, M., Molpro: A General-Purpose Quantum Chemistry Program Package. *Wiley Interdisciplinary Reviews: Computational Molecular Science* **2012**, *2*, 242-253.

26. Frey, R. F.; Davidson, E. R., Potential Energy Surfaces of Ch+4. *J. Chem. Phys.* **1988**, *88*, 1775-1785.

27. Corkum, P. B., Plasma Perspective on Strong Field Multiphoton Ionization. *Phys. Rev. Lett.* **1993**, *71*, 1994-1997.

28. Zhao, S.-F.; Xu, J.; Jin, C.; Le, A.-T.; Lin, C. D., Effect of Orbital Symmetry on the Orientation Dependence of Strong Field Tunnelling Ionization of Nonlinear Polyatomic Molecules. *J. Phys. B* **2011**, *44*, 035601.

29. Tong, X. M.; Zhao, Z. X.; Lin, C. D., Theory of Molecular Tunneling Ionization. *Phys. Rev. A* **2002**, *66*, 033402.

30. Ortiz, J. V., Dyson-Orbital Concepts for Description of Electrons in Molecules. *J. Chem. Phys.* **2020**, *153*, 070902.

31. Spanner, M.; Patchkovskii, S.; Zhou, C.; Matsika, S.; Kotur, M.; Weinacht, T. C., Dyson Norms in Xuv and Strong-Field Ionization of Polyatomics: Cytosine and Uracil. *Phys. Rev. A* **2012**, *86*, 053406.

32. van den Wildenberg, S.; Mignolet, B.; Levine, R. D.; Remacle, F., Temporal and Spatially Resolved Imaging of the Correlated Nuclear-Electronic Dynamics and of the Ionized Photoelectron in a Coherently Electronically Highly Excited Vibrating Lih Molecule. *J. Chem. Phys.* **2019**, *151*, 134310.

33. Condon, E. U., The Franck-Condon Principle and Related Topics. *Am. J. Phys.* **1947**, *15*, 365-374.